



Unidirectional emission of high- Q scarred modes in a rounded D-shape microcavity

Ji-Won Lee,¹ Chang-Hwan Yi,¹ Myung-Woon Kim,² Jinhyeok Ryu,¹ Kwang-Ryong Oh,³ and Chil-Min Kim^{1,*}

¹Department of Emerging Materials Science, DGIST, Daegu 42988, Republic of Korea

²Automation Technology Group, Samsung Electro-Mechanics, Suwon 443-743, South Korea

³IT Convergence and Components Lab. ETRI, Daejeon 34129, South Korea

*chmkim@dgist.ac.kr

Abstract: We propose a deformed microcavity laser, where a high- Q mode group emits unidirectionally. The cavity comprises three circular arcs and one linear section. To minimize diffraction effects from the boundary, three circular arcs and one linear section are tangentially connected. By adjusting the sizes and the positions of the two sub-circular arcs, unidirectionality is maximized. In an experiment with an InP based InGaAsP semiconductor microcavity laser, a lasing mode group localized on a period-7 unstable periodic orbit emits unidirectionally. In our resonance calculation, a high- Q factor is confirmed.

© 2018 Optical Society of America under the terms of the [OSA Open Access Publishing Agreement](#)

Since the report of a microcavity laser generating whispering gallery modes (WGMs) without mirror [1–3], microcavities have attracted a lot of attention because of simplicity of fabrication, a low lasing threshold, and an extremely high quality (Q) factor [4–6]. A WGM is confined along the cavity boundary due to total internal reflection. These properties promise an essential light source for optoelectronic circuits [7] and bio and nanoparticle sensors [8–11].

In spite of many advantages of microcavity lasers supporting high- Q WGMs, there are such drawbacks of isotropic emission direction and low intensity for practical applications. For high emission intensity and directional emission, a chaotic microcavity was proposed [12, 13]. Since then, various deformed microcavities have been extensively studied. Up to now, such microcavities are reported for unidirectional emission as a spiral shaped [14, 15], a rounded isosceles triangular shaped [16], an annular shaped [17], a limaçon shaped [18, 19], a cardioid shaped one [20], an elliptic cavity with a notch [21], and a cavity comprised of two half ellipses [22] and comprised of a half circle and a half quadruple [23, 24].

In these microcavities, while Q -factors are seriously spoiled as deformation increases [12, 25], unidirectionality is guaranteed by proper deformation. Hence, it is considered that there is a trade-off between Q -factors and directionality. Nevertheless, Q -factors of resonances in several deformed microcavities are quite high. As examples, in a limaçon-shaped microcavity, the Q -factor of a transverse magnetic (TM) and a transverse electric (TE) polarized resonance reach up to 10^7 and 1.85×10^5 , respectively, for $nkR \sim 85.5$ [18], where $n = 3.3$ is the effective refractive index, k the free-space wave number, and R the average radius of the cavity. The Q -factor of a TE polarized WGM type resonance in the ellipse with a notch is 5.9×10^5 for $nkR \sim 175$ [21]. The Q -factor of a TE polarized resonance in the cavity comprised of two half ellipses is about 2.85×10^5 for $nkR \sim 120$ [22]. The Q -factor of a TM polarized WGM type resonance in the cavity comprised of a half circle and a half quadrupole is about 5.78×10^6 for $nkR \sim 83.1$ [23]. According to the report of Pascal's limaçon-shaped microcavity [18], the Q -factor of a TE polarized resonance is lower than that of the counterpart TM one due to the Brewster angle. Note that, as mentioned in the above, the Q -factor of the TM mode is about 100 times larger than that of the TE one in [18], Wiersig et al. Strictly speaking, the cavity size should be similar, and the polarization of modes should be the same for a quantitative comparison

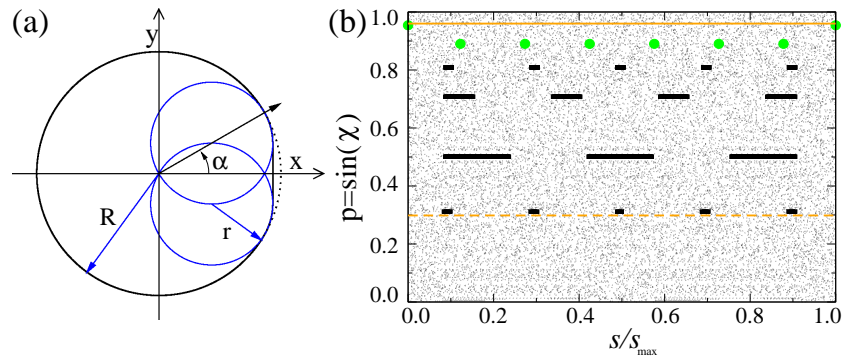


Fig. 1. The design of the cavity and ray dynamics in Birkhoff coordinate. (a) is the shape of the cavity and (b) is the Poincaré surface of section. The thick black lines are marginally unstable periodic orbits. The seven big dots indicate the period-7 unstable periodic orbit, where the lasing modes are localized. The solid line at $p = 0.96$ indicates the outside region of the electrode of our laser and the dashed line at $p = 1/3.3$ is the critical line.

of a Q -factors in different microcavities. Nevertheless, comparing them in qualitative viewpoints is still possible even when these conditions are not fulfilled.

In this paper, we report unidirectional emission of a mode group in a rounded D-shape microcavity (RDM) laser. For experiments, we fabricate an InP based InGaAsP multi-quantum well semiconductor microcavity laser and show unidirectional emission of a TE polarized lasing mode group, which is localized on a period-7 unstable periodic orbit. It is known that the multi-quantum well structured laser emits TE polarized modes. In numerical calculations, the Q -factor of the mode group is about 3.479×10^6 for $nkR \sim 100$. This result implies that although our microcavity is highly chaotic, the Q -factor of a TE polarized resonance is comparable with that of the deformed microcavities in the above.

The design of a RDM is shown in Fig. 1(a). The main circular arc with a radius of $R = 50 \mu\text{m}$ is tangentially connected to two smaller circular arcs with a radius of r at the angle $\pm\alpha$ and a linear section also tangentially connects to two smaller arcs, which satisfies $C^{(1)}$ continuity. In this cavity, the emission depends on two deformation parameters, r and α . For optimal unidirectional emission, we set $r = R/2$ and $\alpha = 30^\circ$. The Poincaré surface of section of ray dynamics in Birkhoff coordinate is shown in Fig. 1(b), which describes successive bounces of rays. In this coordinate, the mapping variables s and $p = \sin \chi$ are a canonical conjugate pair. Here, s is the arc length from the boundary point at x -axis to the point, where a ray bounces on the boundary, and p is the tangential momentum of a ray, whose incident angle is χ . The phase space exhibits no recognizable regular island structures in our simple ray dynamical simulations, and therefore we assumed that our cavity follows the characteristics of fully chaotic systems. The thick black lines are marginally unstable periodic orbits, a one-parameter family of a fragmented resonant torus in perturbed systems, which are in the single torus in integrable systems [26]. The seven big dots indicate the period-7 unstable periodic orbit, where the lasing modes are localized. The solid line at $p = 0.96$ indicates the outside region of the electrode for $R = 50 \mu\text{m}$ and the electrode radius of $48 \mu\text{m}$ and the dashed line at $p = 1/3.3$ is the critical line, which are consistent with the condition of our fabricated laser.

The fabrication steps of our microcavity laser are given as follows: By using metal-organic chemical vapor deposition, an InGaAsP heterostructure is grown on an InP substrate. The multi-quantum well layers are sandwiched by separated confinement heterostructure layers. After the deposition of a multi-quantum well layers, a p-doped InP cladding layer is grown. The active region of the device is composed of seven 0.8% compressive-strained InGaAsP wells

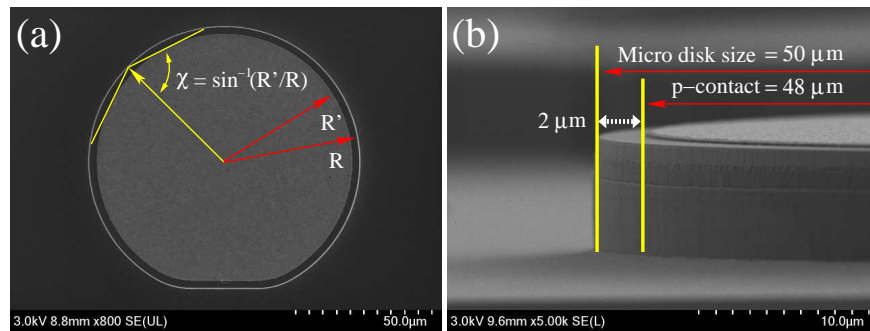


Fig. 2. Scanning electron microscope image of (a) top and (b) side view. R and R' in (a) are the radius of the microdisk and the p-contact electrode which are $50\mu\text{m}$ and $48\mu\text{m}$, respectively. The p-contact electrode defines the area where the injection current is applied into the microdisk. The angle $\chi = \sin^{-1}(48/50 = 0.96)$ in (a) is the lowest incident angle of rays traveling outside of the electrode area. In (b), the vertical lines mark the edge of the cavity and the electrode indicated by the arrows R and R' in (a), and their gap $2\mu\text{m}$ is shown by the bidirectional arrow.

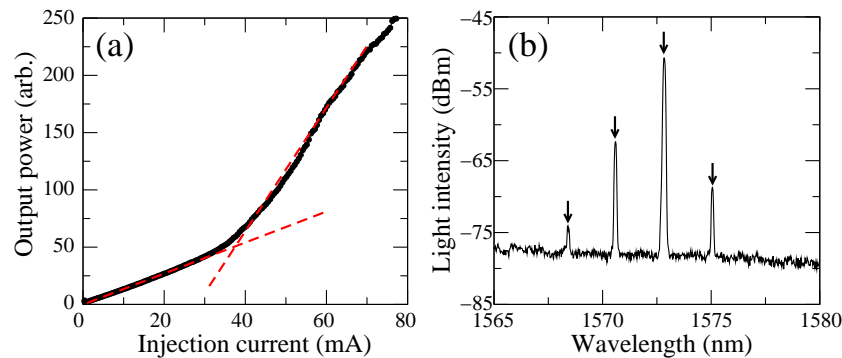


Fig. 3. The emission characteristics of our laser. (a) is the emission intensity depending on the injection current, which shows the threshold around 35 mA which correspond to the lasing threshold current density 0.4835 kA/cm^2 . (b) is the optical spectrum around 1570 nm at 60 mA injection current. There are four lasing modes belonging to a mode group localized on the period-7 unstable periodic orbit.

with a bandgap wavelength of $1.68\mu\text{m}$ and eight 0.6% tensile-strained barriers with a bandgap wavelength of $1.3\mu\text{m}$. The laser heterostructure is completed with a p-doped InGaAs contact layer grown on top of the cladding layer. After the growth, the laser heterostructures are etched into a rounded D-shape cross-section by inductively coupled plasma etching with the cavity radius of $R = 50\mu\text{m}$. The ridge height of the fabricated laser is $6\mu\text{m}$. The etch depth is under the core by more than $4\mu\text{m}$. For excitation, a p-contact metal electrode is defined. The outer edge of the p-electrode follows the perimeter of the microcavity closely along the sidewall with a $2\mu\text{m}$ gap. Figures 2(a) and (b) are the scanning electron microscope image of the top and the side view, respectively.

The laser shown in Fig. 2 is operated in a pulsed current at the 1 MHz repetition rate with a $0.6\mu\text{ sec}$ pulse width to investigate the emission characteristics. In a whole experiment procedure, the temperature is fixed to be 22°C . The laser output is launched into a single mode fiber at $20\mu\text{m}$ apart from the cavity boundary and measured with a power meter connected to a multifunction optical meter. The emission spectrum is measured with an optical spectrum

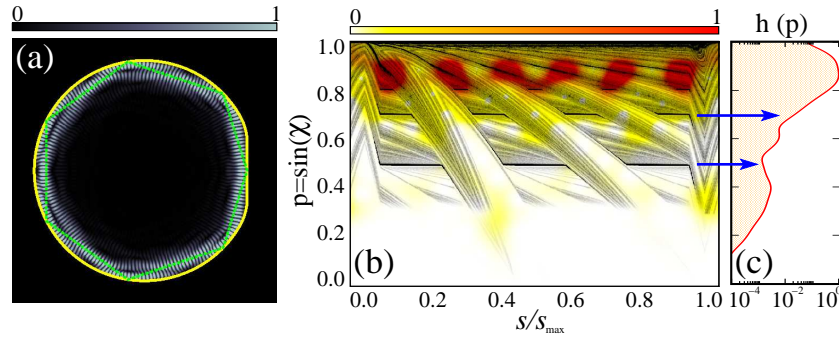


Fig. 4. A resonance localized on the period-7 unstable periodic orbit. (a) is the even resonance, whose eigenvalue is $\text{Re}(nkR) = 100.359$ and $\text{Im}(nkR) = 1.442 \times 10^{-5}$. (b) is the Husimi function $h(s, p)$ superimposed on the survival probability distribution. The main and the minor emission tongue are around $s/s_{max} = 0.4$ and $s/s_{max} = 0.95$, respectively. The Husimi function exhibits localization of the resonance on the period-7 unstable periodic orbit. Weak intensities around the tongues indicate the emission of the resonance by following the unstable manifolds of the chaotic saddle. The green polygonal line in (a) is superimposed on the resonance to guide eyes the period-7 unstable periodic orbit. (c) is the projection of the Husimi distribution on the p -axis. The arrows at $p = 0.5$ and $p = 0.707$ in (c) mark the period-3 and the period-4 MUPOs, respectively. In (b), the Husimi function intensity is in the color-bar scale above the figure while the intensity of the survival probability distribution of the background is in the gray-scale from white to black ranged as 0 to 1.

analyzer. Figure 3(a) shows the emission intensity versus the injection current of a pulse. The figure shows a slope change around 35 mA, which is the lasing threshold. This lasing threshold corresponds to the lasing threshold current density 0.4835 kA/cm^2 taking into account our cavity size. Comparing this value to the ones in the representative previous works, $\sim 0.76 \text{ kA/cm}^2$ in [19], $\sim 0.55 \text{ kA/cm}^2$ [27], $\sim 0.67 \text{ kA/cm}^2$ [28], and $\sim 2.00 \text{ kA/cm}^2$ [29], it reveals that the experimental Q -factor [30] of our laser exhibits a good quality. Above the threshold, the emission intensity linearly increases up to 80 mA. At 60 mA, which is far above the threshold, an emission spectrum is taken as shown in Fig. 3(b). The spectrum exhibits four lasing modes, which are periodic with a equidistance mode spacing of about 2.22 nm. To analyze the lasing modes, the orbit length is obtained by using the equation of $L = \lambda_{avg}^2 / (n_g \Delta\lambda)$, where n_g is the group refractive index of about 3.68 [28] and λ_{avg} is the average wavelength of two neighboring modes. The path length is about $302.4 \mu\text{m}$. When we compare the path length with several orbit lengths, which exist in between the two lines of $p = 0.96$ and $1/3.3$ in Fig. 1(b), the path length well coincide with period-7 unstable periodic orbit within 99.6% accuracy, whose real orbit length is $301.299 \mu\text{m}$.

Because we can not experimentally resolve the Q -factor of the lasing mode group by using our spectrum analyzer, whose resolution is 0.06 nm, we obtain TE polarized resonances around $nkR = 100$ with an effective refractive index $n = 3.3$. Figure 4(a) is an even resonance localized on the period-7 unstable periodic orbit (green polygonal line), which is numerically obtained employing the boundary element method [31], whose eigenvalue is $\text{Re}(nkR) = 100.359$ and $\text{Im}(nkR) = 1.442 \times 10^{-5}$. Although the cavity size in calculation is much smaller than the real one, the Q -factor reaches up to 3.479×10^6 .

The Husimi function [32] of the resonance superimposed on the survival probability distribution is shown in Fig. 4(b). The distribution exhibits ray dynamical emission through unstable manifolds of the chaotic saddle [18, 33–36]. According to the Fresnel's law, the survived intensity of TE polarized rays is accumulated at each phase space cell; our phase space domain, given in the range $(s, p) \in [0, s_{max}] \times [-1, 1]$, is divided into $10^3 \times 10^3$ cells. The survived intensity of

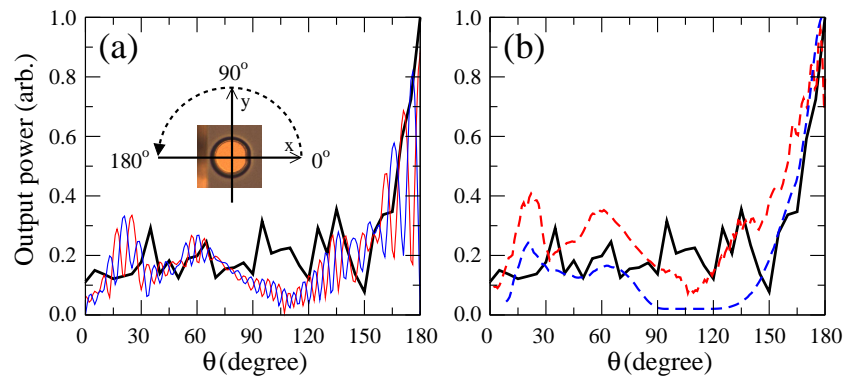


Fig. 5. Far-field patterns. The black curve in (a) and (b) is the experimental data showing the divergence of $\Delta\theta \approx 26^\circ$. (a) is the far-field pattern of an odd resonance (blue) and an even resonance (red). The subemission angles are $\theta \approx 20^\circ$ and 60° . (b) is the ray dynamical far-field pattern (dashed blue), whose divergence angle is $\Delta\theta \approx 26^\circ$ and the summation of the even and the odd resonance (dashed red). The ray dynamics and the summation of the field intensities exhibit subemission directions at around $\theta \approx 20^\circ$ and 60° . The inset in (a) illustrates the angle of far-field measurement.

each cell, where the rays are belonging to, are summed while the rays are undergoing specular reflections at the cavity boundary from 200 times to 250 times (i.e., number of reflections). As time evolves, when the incident angles of rays are less than the critical angle, a part of rays emit out by the Fresnel's law. The distribution exhibits two tongues below the critical line, through which rays escape. The tongues are caused by the trajectories following the unstable manifolds. Because of the symmetry of our cavity, only counter clockwise (CCW) traveling rays are displayed. A tongue around $s/s_{max} = 0.4$ is the main emission gate for unidirectional emission whereas the other around $s/s_{max} = 0.95$ is the minor emission gate for the backward direction with a weak intensity. Similarly, clockwise (CW) rays exhibit the main and the minor emission gate around $s/s_{max} = 0.6$ and 0.05 , respectively. Because the directions of the two main emissions are the same, our microcavity laser is unidirectional. The Husimi function clearly exhibits the localization of the resonance on the period-7 unstable periodic orbit. Although the localization is broad, the main part is below $p = 0.96$. The resonance also follows the unstable manifolds of the chaotic saddle [18, 33–36] and emits out through the tongues as shown by the resonance intensities on the tongues. This phenomenon is well analyzed in terms of the ray-wave correspondence [37, 38] in optical cavity systems. In figure 4(c), the projection of the Husimi distribution on the p -axis as $h(p) = \int_0^1 h(s, p) ds$ is given. The arrowed low intensity points of the Husimi distribution at $p = 0.5$ (period-3 MUPO) and 0.707 (period-4 MUPO) in the figure reveal the evident barrier effects of MUPOs in phase space.

In experiment, we measure the emission direction by rotating the fiber along the cavity boundary at $200 \mu\text{m}$ apart from the boundary. The black curves in Fig. 5 are the experimental far-field pattern (FFP) showing unidirectional emission with the divergence of $\Delta\theta \approx 26^\circ$. Because of the symmetry of our cavity shape, the FFP is displayed only from $\theta = 0^\circ$ to 180° . The experimental FFP is compared with the numerical results of the wave and the ray dynamical FFPs. The FFP of an odd (blue) and an even resonance (red) localized on the period-7 unstable periodic orbit are displayed in Fig. 5(a). Their main emission directions well coincide with each other with the divergence angle of $\Delta\theta \approx 26^\circ$. In the case of the backward emission, there is a slight mismatch between the experiment and the resonances, which is caused by the weak emission intensities at the $200 \mu\text{m}$ distance of the fiber facet.

The ray dynamical FFP (dashed blue) and the FFP of the field intensity summation of the odd

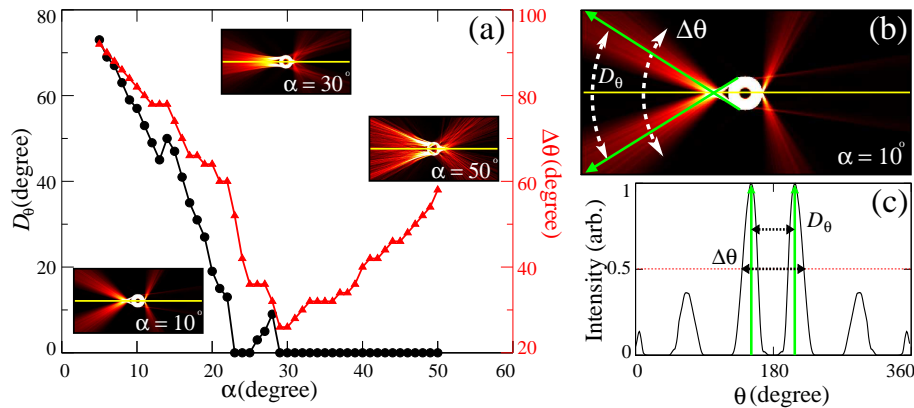


Fig. 6. Emission characteristics of rays depending on α . In (a), the emission direction difference is presented by circles and the full width at half maximum for total divergence is presented by triangles. The left, the center, and the right inset are the emission of rays at $\alpha = 10^\circ$, at 30° , and at 50° , respectively. (b) and (c) show the definitions of the emission direction difference D_θ and the full width at half maximum $\Delta\theta$. Note that in the region $\alpha < 30^\circ$, the emission exhibit two lobes so that $\Delta\theta$ does not give the exact meaning of the full width at half maximum.

and the even resonance (dashed red) are shown in Fig. 5(b). The main emission directions and their divergence angles of the experiment and ray dynamics are almost the same as the divergence angle of $\Delta\theta \approx 26^\circ$. In the case of the backward directions, the FFP of the rays and the wave intensity also well coincide with each other with the emission directions of $\theta \approx 20^\circ$ and 60° . These results indicate that the resonances localized on the period-7 unstable periodic orbit emit unidirectionally with a narrow divergence angle.

For the analysis of the directional emission in a RDM, emission directions depending on the position of two smaller arcs are investigated by using ray dynamics for uniformly distributed initial rays on the whole phase space, i.e., uniformly prepared initial points in phase space (s, p) . In our investigation, when $\alpha < 29^\circ$, CCW and CW traveling rays cross each other to be two emission directions. Hence the emission direction difference D_θ [see Figs. 6(b) and 6(c)] is obtained as shown by the circles in Fig. 6(a) for the distance $100R$ from the cavity boundary, where θ is the emission direction. At $\alpha \approx 25^\circ$ and $\alpha > 29^\circ$, D_θ is almost zero. At $\alpha = 25^\circ$ the CCW and the CW rays cross each other around $100R$ as shown by the inset at $\alpha = 10^\circ$. When $\alpha > 29^\circ$, the emission is unidirectional as shown by the insets at $\alpha = 30^\circ$ and 50° . The full width at half maximum of the total divergence, $\Delta\theta$, is also obtained [see Figs. 6(b) and 6(c)]. As is shown by the triangles in Fig. 6(a), the total divergence angle is minimized at $\alpha = 30^\circ$. Therefore the directionality of our RDM is optimized at $\alpha = \pm 30^\circ$.

In conclusion, we have fabricated a rounded D-shape microcavity laser for $R = 50 \mu\text{m}$. In this microcavity, when the position of two smaller arcs are located at $\alpha = \pm 30^\circ$, the directionality is maximized. Barrier effects of marginally unstable periodic orbits in phase space are uncovered by means of examining a Husimi function distribution along the momentum direction. When the laser is excited by a pulsed current, a single mode group lases, which is localized on the period-7 unstable periodic orbit. The lasing of the mode group is stable up to 80 mA. In our numerical calculations, the Q -factor of an even resonance localized on the periodic orbit reaches 3.479×10^6 for $nkR \approx 100$. Hence we believe that our laser can be used in photonics and optoelectronic applications because our laser can enhance a feasibility of these applications with respect to the coupling efficiency, even in the presence of external perturbations such as a vibration, and the signal discernibility by the unidirectional emission and the high- Q factor, respectively.

Funding

Ministry of Health and Welfare, Republic of Korea (Government-wide R&D Fund project for infectious disease research, HG18C0069).

References

1. C. Garrett, W. Kaiser, and W. Bond, "Stimulated emission into optical whispering modes of spheres," *Phys. Rev.* **124**, 1807 (1961).
2. R. Benner, P. Barber, J. Owen, and R. Chang, "Observation of structure resonances in the fluorescence spectra from microspheres," *Phys. Rev. Lett.* **44**, 475 (1980).
3. S. McCall, A. Levi, R. Slusher, S. Pearton, and R. Logan, "Whispering-gallery mode microdisk lasers," *Appl. Phys. Lett.* **60**, 289–291 (1992).
4. S. Spillane, T. Kippenberg, and K. Vahala, "Ultralow-threshold raman laser using a spherical dielectric microcavity," *Nature* **415**, 621 (2002).
5. D. Armani, T. Kippenberg, S. Spillane, and K. Vahala, "Ultra-high-Q toroid microcavity on a chip," *Nature* **421**, 925 (2003).
6. H. Lee, T. Chen, J. Li, K. Y. Yang, S. Jeon, O. Painter, and K. J. Vahala, "Chemically etched ultrahigh-Q wedge-resonator on a silicon chip," *Nat. Photonics* **6**, 369 (2012).
7. R. K. Chang and A. J. Campillo, *Optical processes in microcavities* (World scientific, 1996).
8. A. M. Armani, R. P. Kulkarni, S. E. Fraser, R. C. Flagan, and K. J. Vahala, "Label-free, single-molecule detection with optical microcavities," *Science* **317**, 783–787 (2007).
9. F. Vollmer and S. Arnold, "Whispering-gallery-mode biosensing: label-free detection down to single molecules," *Nat. Methods* **5**, 591 (2008).
10. J. Zhu, S. K. Ozdemir, Y.-F. Xiao, L. Li, L. He, D.-R. Chen, and L. Yang, "On-chip single nanoparticle detection and sizing by mode splitting in an ultrahigh-Q microresonator," *Nat. Photonics* **4**, 46 (2010).
11. W. Chen, Ş. K. Özdemir, G. Zhao, J. Wiersig, and L. Yang, "Exceptional points enhance sensing in an optical microcavity," *Nature* **548**, 192 (2017).
12. J. U. Nöckel and A. D. Stone, "Ray and wave chaos in asymmetric resonant optical cavities," *Nature* **385**, 45 (1997).
13. C. Gmachl, F. Capasso, E. Narimanov, J. U. Nöckel, A. D. Stone, J. Faist, D. L. Sivco, and A. Y. Cho, "High-power directional emission from microlasers with chaotic resonators," *Science* **280**, 1556–1564 (1998).
14. G. Chern, H. Tureci, A. D. Stone, R. Chang, M. Kneissl, and N. Johnson, "Unidirectional lasing from InGaN multiple-quantum-well spiral-shaped micropillars," *Appl. Phys. Lett.* **83**, 1710–1712 (2003).
15. C.-M. Kim, J. Cho, J. Lee, S. Rim, S. H. Lee, K. R. Oh, and J. H. Kim, "Continuous wave operation of a spiral-shaped microcavity laser," *Appl. Phys. Lett.* **92**, 131110 (2008).
16. M. Kurdoglyan, S.-Y. Lee, S. Rim, and C.-M. Kim, "Unidirectional lasing from a microcavity with a rounded isosceles triangle shape," *Opt. Lett.* **29**, 2758–2760 (2004).
17. J. Wiersig and M. Hentschel, "Unidirectional light emission from high-Q modes in optical microcavities," *Phys. Rev. A* **73**, 031802 (2006).
18. J. Wiersig and M. Hentschel, "Combining directional light output and ultralow loss in deformed microdisks," *Phys. Rev. Lett.* **100**, 033901 (2008).
19. C.-H. Yi, M.-W. Kim, and C.-M. Kim, "Lasing characteristics of a limaçon-shaped microcavity laser," *Appl. Phys. Lett.* **95**, 141107 (2009).
20. I.-G. Lee, S.-M. Go, J.-H. Ryu, C.-H. Yi, S.-B. Kim, K. R. Oh, and C.-M. Kim, "Unidirectional emission from a cardioid-shaped microcavity laser," *Opt. Express* **24**, 2253–2258 (2016).
21. Q. J. Wang, C. Yan, N. Yu, J. Unterhinninghofen, J. Wiersig, C. Pflügl, L. Diehl, T. Edamura, M. Yamanishi, H. Kan, and F. Capasso, "Whispering-gallery mode resonators for highly unidirectional laser action," *Proc. Natl. Acad. Sci.* **107**, 22407–22412 (2010).
22. J. Lee, S. Rim, J. Cho, and C.-M. Kim, "Unidirectional resonance modes supported by secondary islands in a microcavity comprised of two half-ellipses," *Phys. review A* **83**, 033815 (2011).
23. C.-L. Zou, F.-W. Sun, C.-H. Dong, X.-W. Wu, J.-M. Cui, Y. Yang, G.-C. Guo, and Z.-F. Han, "Mechanism of unidirectional emission of ultrahigh Q whispering gallery mode in microcavities," arXiv preprint arXiv:0908.3531 (2009).
24. X.-F. Jiang, Y.-F. Xiao, C.-L. Zou, L. He, C.-H. Dong, B.-B. Li, Y. Li, F.-W. Sun, L. Yang, and Q. Gong, "Highly unidirectional emission and ultralow-threshold lasing from on-chip ultrahigh-Q microcavities," *Adv. Mater.* **24**, OP260–OP264 (2012).
25. H.-H. Yu, C.-H. Yi, and C.-M. Kim, "Mechanism of Q-spoiling in deformed optical microcavities," *Opt. Express* **23**, 11054–11062 (2015).
26. E. G. Altmann, T. Friedrich, A. Motter, H. Kantz, and A. Richter, "Prevalence of marginally unstable periodic orbits in chaotic billiards," *Phys. Rev. E* **77**, 016205 (2008).
27. L. Zhang and E. Hu, "Lasing from InGaAs quantum dots in an injection microdisk," *Appl. Phys. Lett.* **82**, 319–321 (2003).
28. C.-H. Yi, S. H. Lee, M.-W. Kim, J. Cho, J. Lee, S.-Y. Lee, J. Wiersig, and C.-M. Kim, "Light emission of a scarlike mode with assistance of quasiperiodicity," *Phys. Rev. A* **84**, 041803 (2011).

29. C. Yan, Q. J. Wang, L. Diehl, M. Hentschel, J. Wiersig, N. Yu, C. Pflügl, F. Capasso, M. A. Belkin, T. Edamura, M. Yamanishi, and H. Kan, "Directional emission and universal far-field behavior from semiconductor lasers with limaçon-shaped microcavity," *Appl. Phys. Lett.* **94**, 251101 (2009).
30. J. Faist, C. Gmachl, M. Striccoli, C. Sirtori, F. Capasso, D. L. Sivco, and A. Y. Cho, "Quantum cascade disk lasers," *Appl. Phys. Lett.* **69**, 2456–2458 (1996).
31. J. Wiersig, "Boundary element method for resonances in dielectric microcavities," *J. Opt. A: Pure Appl. Opt.* **5**, 53 (2002).
32. M. Hentschel, H. Schomerus, and R. Schubert, "Husimi functions at dielectric interfaces: Inside-outside duality for optical systems and beyond," *Europhys. Lett.* **62**, 636 (2003).
33. E. G. Altmann, "Emission from dielectric cavities in terms of invariant sets of the chaotic ray dynamics," *Phys. Rev. A* **79**, 013830 (2009).
34. E. G. Altmann, J. S. Portela, and T. Tél, "Leaking chaotic systems," *Rev. Mod. Phys.* **85**, 869 (2013).
35. H. G. Schwefel, N. B. Rex, H. E. Tureci, R. K. Chang, A. D. Stone, T. Ben-Messaoud, and J. Zyss, "Dramatic shape sensitivity of directional emission patterns from similarly deformed cylindrical polymer lasers," *J. Opt. Soc. Am. B* **21**, 923–934 (2004).
36. J. Kullig and J. Wiersig, "Frobenius–perron eigenstates in deformed microdisk cavities: non-hermitian physics and asymmetric backscattering in ray dynamics," *New J. Phys.* **18**, 015005 (2016).
37. S. Shinohara, M. Hentschel, J. Wiersig, T. Sasaki, and T. Harayama, "Ray-wave correspondence in limaçon-shaped semiconductor microcavities," *Phys. Rev. A* **80**, 031801 (2009).
38. T. Harayama and S. Shinohara, "Ray-wave correspondence in chaotic dielectric billiards," *Phys. Rev. E* **92**, 042916 (2015).